

Target Localization and Performance Trade-Offs in Cooperative ISAC Systems: A Scheme Based on 5G NR OFDM Signals

Zhenkun Zhang, Hong Ren, Cunhua Pan, Sheng Hong, Dongming Wang, Jiangzhou Wang, *Fellow, IEEE*, and Xiaohu You, *Fellow, IEEE*

Abstract—The integration of sensing capabilities into communication systems, by sharing physical resources, has a significant potential for reducing spectrum, hardware, and energy costs while inspiring innovative applications. Cooperative networks, in particular, are expected to enhance sensing services by enlarging the coverage area and enriching sensing measurements, thus improving the service availability and accuracy. This paper proposes a cooperative integrated sensing and communication (ISAC) framework by leveraging information-carrying orthogonal frequency division multiplexing (OFDM) signals transmitted by access points (APs). Specifically, we propose a two-stage scheme for target localization, where communication signals are reused as sensing reference signals based on the system information shared at the central processing unit (CPU). In Stage I, we measure the ranges of scattered paths induced by targets, through the extraction of time-delay information from the received signals at APs. Then, the target locations are estimated in Stage II based on these range measurements. Considering that the scattered paths corresponding to some targets may not be detectable by all APs, we propose an effective algorithm to match the range measurements with the targets and achieve the target location estimation. Notably, by analyzing the OFDM numerologies defined in fifth generation (5G) standards, we elucidate the flexibility and consistency of performance trade-offs in both communication and sensing aspects. Finally, numerical results confirm the effectiveness of our sensing scheme and the cooperative gain of the ISAC framework.

Index Terms—Cooperative integrated sensing and communication (ISAC), orthogonal frequency division multiplexing (OFDM), Cell-free MIMO, bistatic localization.

I. INTRODUCTION

Driven by the emerging services requiring high-level communication and sensing capabilities, e.g., vehicle to everything (V2X), extended reality and smart home, integrated sensing and communication (ISAC) has been envisioned as a pivotal technology for the sixth generation (6G) wireless networks [1]. By sharing core hardware, space-time-frequency resources and/or transmit signals within a single system in a symbiotic manner, ISAC networks are able to improve the spectral and energy efficiencies, while reducing the hardware scale and costs [2]. In addition, mutual enhancement for both communication and sensing performance is expected to be achieved by

the coexistence of the two functionalities. For example, the transmission rate and robustness of wireless communication systems can be enhanced with the knowledge of propagation environment [3].

Depending on the employed waveform, ISAC schemes can be classified into two primary categories: sensing-centric and communication-centric. Sensing-centric schemes manipulate the radar signals, enabling the modulation of a limited number of bits [4], [5]. Nevertheless, the communication capabilities of these sensing-centric ISAC systems are extremely constrained due to the reduction in signal autocorrelation caused by high-order random symbol modulation. Hence, they are unable to meet the data throughput demands of various ISAC applications. In contrast, the communication-centric ISAC schemes focus on the implementation of sensing functionality based on the communication signals. Then, the use case of the communication system can be largely expanded beyond data transmissions, realizing applications such as localization and tracking, environment sensing, gesture and activity recognition, which can also be triggers for potential novel applications [6], [7]. An intuitive advantage of communications-centric ISAC scheme is its potential to leverage the widespread deployment of numerous communication nodes, such as base stations (BSs), WiFi routers and user equipments (UEs), for sensing [8]. This greatly reduces the difficulty and cost of ISAC system deployment, especially in indoor and complex urban scenarios. Moreover, the communication network-based ISAC system can benefit from the cooperation between the communication nodes [9]. Thanks to the wider distribution area of and/or dense deployment of communication nodes, the cooperative ISAC networks hosts abundant sources of sensing measurements and computing capability [10], [11], enabling high performance in terms of coverage range, sensing accuracy, robustness, flexibility, and so on [12].

For the UEs equipped with signal transmission capabilities and registered within communication networks, their locations can be efficiently estimated by employing the established *device-based* sensing methodologies [13]. These methodologies involve the extraction of sensing measurements, such as time-of-arrival and angle-of-arrival, from dedicated reference signals exchanged between UEs and BSs. However, for passive targets not interconnected within the communication networks, the adoption of a *device-free* sensing approach becomes imperative. Similar to conventional radar systems, device-free sensing schemes detect, localize and/or track targets solely by analysing the communication signals received at the receivers,

Zhenkun Zhang, Hong Ren, Cunhua Pan, Dongming Wang and Xiaohu You are with National Mobile Communications Research Laboratory, Southeast University, Nanjing 210096, China (e-mail: zhenkun_zhang, hren, cpan, wangdm, xhyu@seu.edu.cn).

Sheng Hong is with the Information Engineering School, Nanchang University, Nanchang, Jiangxi 330031, China (e-mail: shenghong@ncu.edu.cn).

Jiangzhou Wang is with the School of Engineering, University of Kent, CT2 7NZ Canterbury, U.K. (e-mail: j.z.wang@kent.ac.uk).

which constitute reflections from the targets. This thus motivates our work on the development of novel methods for device-free sensing.

The primary obstacle in implementing device-free sensing within communication networks arises from the unfavourable radar sensing characteristics inherent in the random waveforms required for data transmission [14]. Notably, orthogonal frequency division multiplexing (OFDM) is the predominant waveform for 5G cellular networks and a prominent candidate waveform for 6G. To address this issue, several studies have explored device-free sensing methods for OFDM-based cellular networks. A sensing framework was designed in [15], where the BS searches candidate sensing targets using a rotating beam to scan the service area. Based on the echoes of multiple input multiple-output (MIMO)-OFDM communication signals with *cyclic prefix* (CP), a preliminary two-stage framework for sensing measurement extraction and multi-target localization was proposed in [16]. By utilizing the positioning reference signal (PRS) in 5G new radio (NR) standards as a sensing reference signal, the authors of [17] proposed a sensing scheme for passive targets and analyzed its performance for range and velocity estimation. In [18], a signal-stripping-based approach for sensing parameter estimation was designed, leveraging estimated data symbols and channels. However, the aforementioned studies only focused on the sensing approaches for each communication node, without considering the cooperative gain on sensing performance of the entire ISAC system.

Utilizing networked nodes in communication systems, cooperative sensing is expected to satisfy the need of practical applications for large-coverage, precise and robust sensing [19]. Therefore, the cooperative interactions among communication nodes has been explored in a few contributions from the following aspects.

- 1) *Cooperation framework*: In [20], a frame structure design was proposed to facilitate reference-signal-based sensing among BSs in adjacent communication cells. Note that the parameters for synchronization, extracted sensing measurements, and signals exchanged between nodes can serve as prior information for target sensing. Information sharing and data fusion are highly necessary for cooperative sensing tasks. Thus, the networks with centralized signal processing architecture are ideal platforms for the ISAC systems. Based on the cloud radio access network (C-RAN) architecture [21], the authors of [22] proposed a scheme for sensing parameter extraction and clutter reduction by developing a general signal model for both uplink and downlink orthogonal frequency-division multiple access (OFDMA) MIMO signals.
- 2) *Performance analysis and transmission design*: Investigating a rate-splitting scheme for C-RAN-based ISAC systems, the authors of [23] optimized communication and sensing performance by analyzing the Pareto boundary of the performance region. Cell-free MIMO network, in which multiple distributed access points (APs) are connected to a central processing unit (CPU) via high-capacity fronthaul links, emerged as a scalable version of C-RAN [24]. Recently, the authors of [25] studied the

cell-free massive MIMO ISAC system, focusing on the optimization of user scheduling and power allocation.

- 3) *Sensing algorithm design*: In [26]–[28], algorithms for joint data association and target localization were designed for the corresponding cooperative sensing schemes. By extending the ISAC framework in [16] to a multi-BS cellular network, the scheme in [26] estimated target locations using range measurements obtained by the BSs. The authors of [27] proposed a trilateration sensing scheme for a two-BS network with the assistance of a reconfigurable intelligent surface. For the localization and velocity estimation of a moving target, the scheme in [28] fused the phase features that are extracted from the demodulation symbols of BSs.

The design of algorithms for target sensing, particularly regarding data fusion, is a key issue in implementing ISAC systems. Nevertheless, the sensing schemes in [26]–[28] assumed that each target is detectable by all cooperative nodes, limiting the coverage area of the entire ISAC system, especially when the number of nodes is large. Moreover, each node in these schemes is required to transmit signals and receive the echoes in a full-duplex manner, leading to self-interference that cannot be completely mitigated using the existing methods.

In this paper, we focus on the design of practical cooperative ISAC framework that are compatible with the 5G and beyond cellular networks. We consider a cell-free MIMO network as the cooperation architecture, where multiple APs and UEs exchange communication signals, while the received downlink signals are reused as sensing reference signals for target localization. This design minimizes the modification to the existing wireless communication systems, without requiring full-duplex operation of the APs. To achieve the device-free sensing based on the practical OFDM communication signals, effective signal processing method is proposed to extract range measurements and estimate the locations of targets. Furthermore, the performance trade-offs for communication and sensing tasks are revealed base on numeral analysis. The main contributions of this paper are summarized as follows:

- 1) Firstly, we propose a novel cooperative ISAC framework based on a cell-free network consisting of multiple communication APs. Inspired by the frame structure employed in wireless communications, the framework facilitates cell-free target localization without relying on dedicated sensing reference signals. Based on the comprehensive information sharing at the CPU, our proposed scheme achieves target sensing solely utilizing the received information-bearing OFDM signals that are transmitted from other APs and reflected by the targets without sacrificing communication performance.
- 2) Secondly, we propose an efficient two-stage scheme for cooperative device-free target localization. We consider the signal model of the commonly used OFDM symbol with CP. Note that the passive targets introduce scattered paths among the APs. In the first stage, by estimating the delayed taps of the multi-path channels, the length of the AP-target-AP scattered paths are estimated based on the received communication signals. The estimations of path

TABLE I
SUPPORTED OFDM NUMEROLOGIES AND CORRESPONDING FRs [29]

μ	CP	FR(s)	N_f
0, 1	Normal	FR1	4096
2	Normal, Extended	FR1, FR2	
3 - 6	Normal	FR2	

length are equivalent to *bistatic range measurements* in radar systems, and are utilized in the second stage for the location estimation of each target. Specifically, we propose an algorithm based on the maximum-likelihood (ML) method to jointly associate each range measurement with correct target and estimate the target locations. In particular, the proposed sensing scheme eliminates the need for complete target coverage by every AP, allowing the ISAC coverage area to expand with the increasing number of cooperative APs.

- 3) Thirdly, we discuss the performance trade-offs achievable in practical cell-free cooperative ISAC systems. Utilizing the transmission configurations specified in the Third Generation Partnership Project (3GPP) standard, we demonstrate flexible trade-offs among various key performance indicators (KPIs) for communication and sensing applications. Furthermore, by extending the ISAC system to general scenarios, we reveal additional degrees of freedom (DoF) for these trade-offs.
- 4) Finally, based on extensive simulation results, we validate the effectiveness of the proposed cooperative ISAC framework and sensing scheme. Insights about the performance of ISAC systems are also derived from the simulation results, providing guidance for engineering practice.

The remainder of this paper is organized as follows. Section II introduces the frame structure of 5G. Section III describes the proposed cooperative ISAC framework and the signal model. In Section IV, we develop a sensing scheme to extract range measurements and estimate the locations of targets. In Section V, the trade-offs in practical cooperative ISAC systems are analyzed and the sensing scheme is modified for general scenarios. Extensive simulation results and discussions are given in Section VI. Finally, Section VII draws the conclusions of this work.

Notations: \mathbb{C} and $j = \sqrt{-1}$ denote the complex field and the imaginary unit, respectively. Vectors, matrices and sets are represented as boldface lowercase, boldface uppercase and calligraphic uppercase letters, respectively. For a matrix \mathbf{A} , its transpose and Hermitian are denoted by \mathbf{A}^T , \mathbf{A}^H , respectively. For a vector \mathbf{a} , $\|\mathbf{a}\|_1$ and $\|\mathbf{a}\|_2$ respectively denote its l_1 - and l_2 -norm, and $\text{diag}(\mathbf{a})$ denotes a diagonal matrix where the elements of \mathbf{a} form the main diagonal elements of the matrix. For a set \mathcal{A} , $|\mathcal{A}|$ denotes the number of elements in \mathcal{A} .

II. 5G NR FRAME STRUCTURE

In this section, we review the frame structure specified in 3GPP standard for 5G NR, focusing on the resource allocations between CP and data symbols.

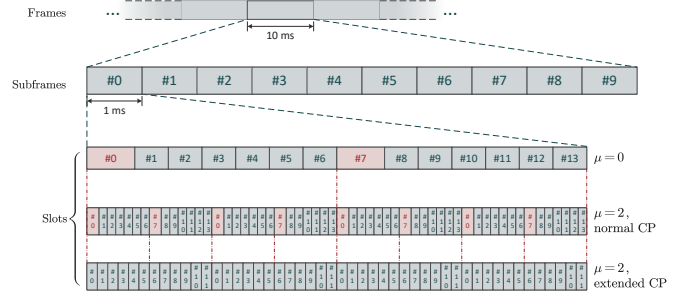


Fig. 1. Transmission organization in 5G NR.

A. Numerologies

An OFDM symbol is the smallest time-domain resource unit in 5G NR, and a CP is inserted at the beginning of each OFDM symbol. According to 3GPP TS 38.211 Release 17 [29], the OFDM numerologies refer to the configurations of subcarrier spacing (SCS) and CP. Specifically, there are seven supported configurations of SCS Δf^μ given as follows:

$$\Delta f^\mu = 2^\mu \times 15 \text{ [KHz]}, \quad (1)$$

where $\mu \in \{0, 1, \dots, 6\}$ is the configuration parameter, while the optional CP configurations include two modes: *normal* and *extended*.

The frequency bands available to NR are divided into two frequency ranges (FRs), namely FR1 (0.41 GHz - 7.125 GHz) and FR2 (24.25 GHz - 52.6 GHz) [30]. The SCS configurations applicable to each FR are summarized in Table I. In addition, the fast Fourier transform (FFT) size, which is also the number of samples in a time-domain OFDM symbol without CP, is fixed at $N_f = 4096$. Hence, the sampling interval of SCS configuration μ is

$$T_s^\mu = \frac{1}{N_f \Delta f^\mu \times 10^3} = \frac{1}{2^{\mu+12} \times 15 \times 10^3} \text{ [s]}. \quad (2)$$

The normal CP can be used with all SCS configurations, while the extended CP is dedicated to the configuration with 60 KHz SCS in high delay spread transmission. The CP configurations affect the position and duration of the CP for each OFDM symbol, which will be detailed in the next subsection.

B. Structure of Frames, Subframes and Slots

As illustrated in Fig. 1, the transmission in NR is organized in frames with duration of 10 milliseconds (ms), each of which is divided into ten 1 ms-duration subframes. Then, each subframe is equally divided into 2^μ slots. As shown in Table II, each slot consists of N_{symp} consecutive OFDM symbols numbered $l_s \in \{0, \dots, N_{\text{symp}} - 1\}$ in increasing order with $N_{\text{symp}} = 14$ for normal CP and $N_{\text{symp}} = 12$ for extended CP. Hence, the number of OFDM symbols in a frame is equal to $10 \times 2^\mu \times N_{\text{symp}}$. From (1), it can be observed that the number of transmitted OFDM symbols in a given duration increases with respect to (w.r.t.) SCS, resulting in a higher maximum data rate.

As specified in TS 38.211, the time unit is defined as $T_c = 1/(480 \times 10^3 N_f)$ s. For each configuration μ , the duration of

TABLE II
5G NR STRUCTURE OF FRAMES, SUBFRAMES AND SLOTS [29]

CP	μ	Number of symbols per slot N_{symb}	CP duration per symbol T_{CP}^{μ, l_s} [ms]	CP duration per symbol Q_{CP}^{μ, l_s} [sampling interval]
Normal	0 - 6	14	$\begin{cases} 0.3 \times 2^{-\mu-6} + 1/1920 & l_s \in \{0, 7\} \\ 0.3 \times 2^{-\mu-6} & \text{others} \end{cases}$	$\begin{cases} 288 + 2^{\mu+5} & l_s \in \{0, 7\} \\ 288 & \text{others} \end{cases}$
Extended	2	12	4.17×10^{-3}	1024

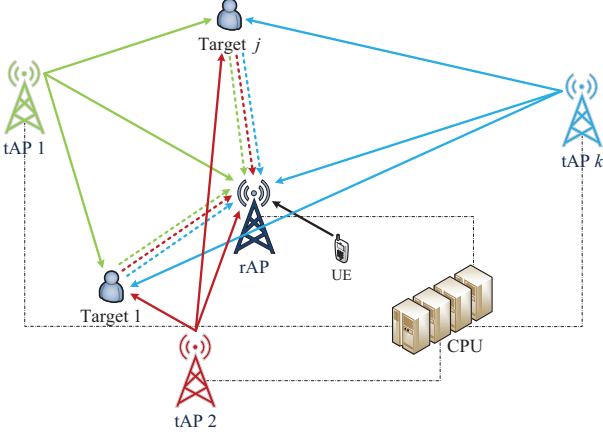


Fig. 2. System model for a cell-free cooperative ISAC system with K tAPs and J targets.

CP in time units is specified as follows [29]

$$N_{\text{CP}}^{\mu, l_s} = \begin{cases} 512\kappa \times 2^{-\mu} & \text{extended CP} \\ 144\kappa \times 2^{-\mu} + 16\kappa & \text{normal CP, } l_s \in \{0, 7\}, \\ 144\kappa \times 2^{-\mu} & \text{normal CP, } l_s \notin \{0, 7\} \end{cases} \quad (3)$$

where $\kappa = 64$. That is, the CP duration for each symbol in terms of time T_{CP}^{μ, l_s} is given by $N_{\text{CP}}^{\mu, l_s} T_c$. Meanwhile, the CP duration in terms of the number of sampling intervals Q_{CP}^{μ, l_s} is shown in Table II. For simplicity, we will replace Q_{CP}^{μ, l_s} with Q in the remainder of this paper.

III. SYSTEM MODEL

In this section, we propose an ISAC framework based on the cell-free MIMO networks. The system architecture and signal model are presented.

A. Cell-Free Cooperative ISAC System

Consider an OFDM-based cooperative ISAC system, which is developed upon a cell-free MIMO network consisting of multiple single-antenna APs as shown in Fig. 2. To mitigate the interference caused by the dense deployment, the APs are assumed to operate on non-overlapping frequency bands, and thus the signals from different APs can be distinguished by applying bandpass filtering operations. Through fronthaul links, the APs are connected with a CPU, at which the signals transmitted and received by all APs are processed in a centralized manner. This configuration facilitates the sharing of comprehensive network information, such as the AP

locations, synchronization parameters and the signal data. The cooperative ISAC system operates on time division duplexing (TDD) mode, which is the sole duplex mode employed for cellular network at frequency bands exceeding 3 GHz as per 5G NR standards [30]. Based on the flexible slot formats [31], the uplink/downlink transmissions can be finely scheduled. In this context, we assume that in the duration of a given OFDM symbol, there is one active receiver AP (rAP) along with K active transmitter APs (tAPs), and the selection of rAP can be dynamically switched. Owing to the real-time sharing of the network information, the information-bearing signals transmitted by the tAPs can be utilized by the rAP as pilot signals. Similar to bistatic radar, the time-delay information for scattered paths in the channels can be extracted from the received signals. In this work, we focus on the target localization based on the OFDM communication signals in the cooperative ISAC scenario, as well as the performance trade-offs based on the NR frame structure.

B. Signal Transmission Model

It is assumed that the transmit power p , the SCS Δf^μ and the number of subcarriers N_c allocated for each AP are the same. Let us denote $s_{k,i}$ as the symbol that modulates the i -th subcarrier, $i = 0, 1, \dots, N_c - 1$, allocated for tAP k . Then, by operating zero padding for IFFT, the frequency-domain OFDM symbol transmitted from tAP k can be denoted by

$$\mathbf{s}_k = [0, \dots, 0, s_{k,0}, \dots, s_{k,N_c-1}, 0, \dots, 0]^T \in \mathbb{C}^{N_f \times 1}. \quad (4)$$

Then, the baseband time-domain OFDM symbol transmitted from tAP k is expressed as

$$\mathbf{x}_k \triangleq [x_{k,0}, \dots, x_{k,N_f-1}]^T = \sqrt{p} \mathbf{W} \mathbf{H} \mathbf{s}_k, \quad (5)$$

where $\{x_{k,n}\}_{n=0}^{N_f-1}$ are the samples of the time-domain OFDM symbol and $\mathbf{W} \in \mathbb{C}^{N_f \times N_f}$ is the discrete Fourier transform (DFT) matrix with its entries given by

$$[\mathbf{W}]_{i,j} = \frac{1}{\sqrt{N_f}} e^{-j \frac{2\pi}{N_f} ij}, \quad i, j = 0, 1, \dots, N_f - 1. \quad (6)$$

After inserting the CP, the overall baseband time-domain OFDM symbol transmitted by tAP k is given by

$$\begin{aligned} \bar{\mathbf{x}}_k &\triangleq \left[\underbrace{\bar{x}_{k,-Q}, \dots, \bar{x}_{k,-1}}_{\text{CP}}, \bar{x}_{k,0}, \dots, \bar{x}_{k,N_f-1} \right]^T \\ &= \left[\underbrace{x_{k,N_f-Q}, \dots, x_{k,N_f-1}}_{\text{CP}}, x_{k,0}, \dots, x_{k,N_f-1} \right]^T, \quad (7) \end{aligned}$$

where $\{\bar{x}_{k,n}\}_{n=-Q}^{N_f-1}$ denote the samples of the overall baseband time-domain OFDM symbol attached with CP, which satisfy

$$\bar{x}_{k,n} = x_{k,(n \bmod N_f)}, \quad n \in [-Q, N_f - 1], \quad (8)$$

$$\bar{x}_{k,n} = \bar{x}_{k,n+N_f}, \quad n \in [-Q, -1], \quad (9)$$

where the operation mod returns the remainder of division.

Let $\mathbf{h}_k = [h_{k,0}, h_{k,1}, \dots, h_{k,L-1}]^T$ denote the multi-path channel between tAP k and the rAP, where L satisfying $L-1 \leq Q$ is the number of channel impulse response taps and $h_{k,l}$ represents the channel at the (delayed) tap with a delay of l sampling intervals. Due to the intersymbol interference caused by multi-path effect, when $\bar{x}_{k,n}$ arrives at the rAP through $h_{k,0}$, the sampled value of received baseband time-domain signal, denoted by $y_{k,n}$, is given by

$$y_{k,n} = \sum_{l=0}^{L-1} h_{k,l} \bar{x}_{k,n-l} + z_n, \quad n = -Q, \dots, N_f - 1, \quad (10)$$

where $z_n \sim \mathcal{CN}(0, \sigma_z^2)$ denotes the circularly symmetric complex Gaussian (CSCG) noise at the n -th sample. Recall that the APs operate on non-overlapping frequency bands. The uplink signals received at the rAP from the UEs are orthogonal to the downlink signals from the tAPs in the frequency-domain. Consequently, the former signals are filtered out from $y_{k,n}$ and, therefore, omitted in (10). The corresponding signal vector of (10) can be denoted as

$$\bar{\mathbf{y}}_k = [\bar{\mathbf{y}}_k^{(1),T}, \bar{\mathbf{y}}_k^{(2),T}]^T, \quad (11)$$

with

$$\bar{\mathbf{y}}_k^{(1)} = [y_{k,-Q}, \dots, y_{k,L-Q-2}]^T, \quad (12)$$

$$\bar{\mathbf{y}}_k^{(2)} = [y_{k,L-Q-1}, \dots, y_{k,N_f-1}]^T. \quad (13)$$

We can observe that $\bar{\mathbf{y}}_k^{(2)}$ is not related to the samples in previous and subsequent OFDM symbols. Therefore, after the rAP discards the first Q samples of $\bar{\mathbf{y}}_k$, the intersymbol interference is eliminated. Denote by $\mathbf{y}_k = [y_{k,0}, \dots, y_{k,N_f-1}]^T$ the resulting baseband time-domain received signal. From (8) and (10), we have

$$y_{k,n} = \sum_{l=0}^{L-1} h_{k,l} \bar{x}_{k,((n-l) \bmod N_f)} + z_n, \quad n = 0, \dots, N_f - 1. \quad (14)$$

Then, by defining $\bar{\mathbf{h}}_k = [h_{k,0}, h_{k,1}, \dots, h_{k,L-1}, 0, \dots, 0]^T \in \mathbb{C}^{N_f \times 1}$ as the delayed tap vector, $y_{k,n}$ can be expressed as

$$\mathbf{y}_k = \bar{\mathbf{h}}_k \otimes \mathbf{x}_k + \mathbf{z}, \quad (15)$$

where \otimes denotes the *cyclic convolution* operation and $\mathbf{z} = [z_0, \dots, z_{N_f-1}]^T \sim \mathcal{CN}(0, \sigma_z^2 \mathbf{I}_{N_f})$. Then, the frequency-domain received OFDM symbol $\hat{\mathbf{s}}_k$ from tAP k is given by

$$\hat{\mathbf{s}}_k \triangleq [\hat{s}_{k,0}, \dots, \hat{s}_{k,N_f-1}]^T = \mathbf{W} \mathbf{y}_k, \quad \forall k. \quad (16)$$

In the following, we reformulate (16) as a function of \mathbf{s}_k .

By utilizing the property of DFT, we have

$$\begin{aligned} \hat{\mathbf{s}}_k &= \mathbf{W} \mathbf{y}_k = \text{DFT}(\bar{\mathbf{h}}_k \otimes \mathbf{x}_k + \mathbf{z}) \\ &= \sqrt{N_f} \text{DFT}(\bar{\mathbf{h}}_k) \odot \text{DFT}(\mathbf{x}_k) + \mathbf{W} \mathbf{z}, \end{aligned} \quad (17)$$

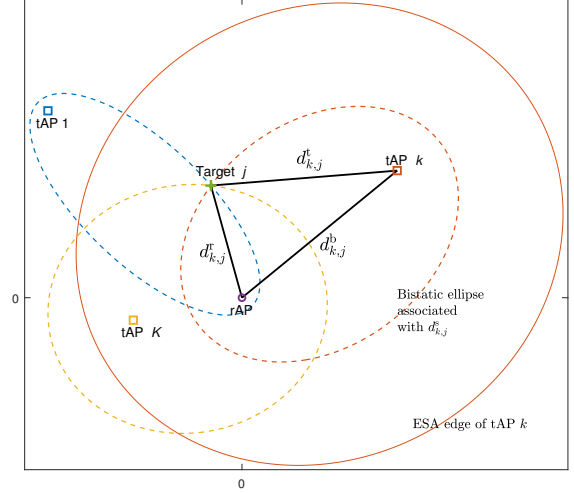


Fig. 3. Illustration of bistatic ranges corresponding to Target j .

where \odot denotes the Hadamard product operation. It can be readily verified that the n -th element of $[\sqrt{N_f} \text{DFT}(\bar{\mathbf{h}}_k)]$, denoted by $\lambda_{k,n}$, is given by

$$\lambda_{k,n} = \sum_{l=0}^{L-1} h_{k,l} \exp\left(\frac{-j2\pi nl}{N_f}\right), \quad n = 0, 1, \dots, N_f - 1. \quad (18)$$

Define a diagonal matrix $\mathbf{\Lambda}_k = \text{diag}(\lambda_{k,1}, \dots, \lambda_{k,N_f})$. Note that $\mathbf{W}^H \mathbf{W} = \mathbf{I}$. We can further derive from (17) that

$$\begin{aligned} \hat{\mathbf{s}}_k &= \mathbf{\Lambda}_k \mathbf{W} \mathbf{x}_k + \mathbf{W} \mathbf{z} \\ &= \sqrt{p} \mathbf{\Lambda}_k \mathbf{s}_k + \mathbf{W} \mathbf{z} \\ &\triangleq \sqrt{p} \text{diag}(\mathbf{s}_k) \mathbf{C} \mathbf{h}_k + \hat{\mathbf{z}}, \end{aligned} \quad (19)$$

where $\hat{\mathbf{z}} = \mathbf{W} \mathbf{z} \sim \mathcal{CN}(0, \sigma_z^2 \mathbf{I}_N)$ and the (n, l) -th element of $\mathbf{C} \in \mathbb{C}^{N_f \times L}$ is given by

$$[\mathbf{C}]_{n,l} = \exp\left(\frac{-j2\pi nl}{N_f}\right). \quad (20)$$

As shown in (19), the received OFDM symbol $\hat{\mathbf{s}}_k$ at the rAP is also a function w.r.t. channel \mathbf{h}_k in a linear form.

IV. COOPERATIVE SENSING SCHEME

In this section, we apply the two-stage framework for the device-free localization of the passive targets. Specifically, the length of the scattered path related to each target is firstly estimated, and the results are used in Stage II for target localization.

A. Stage I: Bistatic Range Measurement

In this stage, the *bistatic ranges*, i.e., the ranges of the tAP-target-rAP scattered paths, are estimated by extracting the time-delay information from channel \mathbf{h}_k 's. Without loss of generality, we assume that the rAP is located at (0,0) as shown in Fig. 3. The coordinates of tAP k and Target j are denoted by $\mathbf{a}_k = [a_k^x, a_k^y]^T$ and $\mathbf{q}_j = [q_j^x, q_j^y]^T$, respectively, where the values of \mathbf{a}_k 's are known at the CPU. Therefore, the distance between tAP k and Target j can be calculated

as $d_{k,j}^t = \|\mathbf{q}_j - \mathbf{a}_k\|_2$ and that between Target j and the rAP is $d_{k,j}^r = \|\mathbf{q}_j\|_2$. The bistatic range corresponding to Target j and tAP k is represented as $d_{k,j}^s = d_{k,j}^t + d_{k,j}^r$. The direct path range, also known as the *baseline range*, between tAP k and the rAP is given by $d_k^b = \|\mathbf{a}_k\|_2$.

We assume that the signal scattered by more than one target is too weak to be detected. Since the tAPs are typically deployed at open areas, there is a line-of-sight (LoS)-dominant channel $h_{k,0}$ between tAP k and the rAP. By contrast, the scattered paths satisfy $h_{k,l} = 0$ for $l \geq 1$ unless some targets exist. Let us define a vector $\hat{\mathbf{h}}_k = [h_{k,1}, \dots, h_{k,L-1}]^T$ consisting of the last $L-1$ elements of \mathbf{h}_k . Then, $\hat{\mathbf{h}}_k$ possesses a sparsity when the number of targets is much smaller than L , and thus can be estimated by the least absolute shrinkage and selection operator (LASSO) [32] technique. Specifically, the LASSO problem is formulated as follows

$$\min_{\hat{\mathbf{h}}_k} \frac{1}{2} \|\hat{\mathbf{s}}_k - \sqrt{p} \text{diag}(\mathbf{s}_k) \mathbf{C} \hat{\mathbf{h}}_k\|_2^2 + \varepsilon \|\hat{\mathbf{h}}_k\|_1, \quad (21)$$

where $\varepsilon \geq 0$ is a penalty factor. When ε takes a large value, each element in the optimal solution of Problem (21) tends towards zero, which enhances the sparsity of $\hat{\mathbf{h}}_k$ but may lead to the neglect of some scattered paths. In practice, a good trade-off between the measurement accuracy and channel sparsity may be achieved by gradually increasing ε [16]. Problem (21) is a convex problem, which can be optimally solved by the optimization tools such as CVX [33].

Suppose that Target j induces a scattered path with $h_{k,l} \neq 0$ for some $l \geq 1$. Then, the signal will experience a delay of l OFDM sampling intervals more than the LoS path when propagated through this scattered path. Hence, the bistatic range corresponding to Target j satisfies

$$(l-1)\Delta d^s + d_k^b < d_{k,j}^s \leq l\Delta d^s + d_k^b, \quad (22)$$

where $\Delta d^s \triangleq c_0 T_s^\mu$ with c_0 being the speed of light is defined as the *bistatic range resolution*, which indicates the worst-case bistatic range measurement error. Specifically, $d_{k,j}^s$ can be approximated as the mid-point of the range in (22) with a measurement error not exceeding $\Delta d^s/2$:

$$\hat{d}_{k,j}^s = \left(l - \frac{1}{2}\right) \Delta d^s + d_k^b, \quad l = 1, \dots, L-1. \quad (23)$$

In this work, we assume that the spacing between the targets is relatively large, allowing the scattered paths induced by any two targets to be distinguished. After the measurement of $d_{k,j}^s$'s, the CPU obtains a set of bistatic range measurements corresponding to each tAP:

$$\mathcal{D}_k = \left\{ \hat{d}_{k,j}^s \mid \forall l \geq 1 \text{ satisfying } h_{k,l} \neq 0 \right\}, \quad \forall k. \quad (24)$$

Denote the number of targets by J . Suppose that Target j is located far from tAP k and the rAP such that the introduced scattered path is much longer than the LoS path. In this case, due to the limited duration of CP, the bistatic range $d_{k,j}^s$ cannot be measured by extracting the time-delay information, and thus $\hat{d}_{k,j}^s = \emptyset$. In the following, we derive the edge of the *effective sensing area* (ESA) of each tAP, wherein the bistatic range corresponding to a target can be measured. As illustrated in

Fig. 3, we define the *bistatic ellipse* associated with the bistatic range $d_{k,j}^s$ as the ellipse that satisfies: 1) its foci are located at $(0, 0)$ and \mathbf{a}_k , and 2) the equation $\|\mathbf{q}\|_2 + \|\mathbf{q} - \mathbf{a}_k\|_2 = d_{k,j}^s$ holds for any point \mathbf{q} on the ellipse. From (22), the ESA of tAP k is the area enclosed by the bistatic ellipse associated with the following bistatic range

$$d_{k,j}^{s,\max} = Q\Delta d^s + d_k^b. \quad (25)$$

From the above discussion, we have $|\mathcal{D}_k| \leq J, \forall k$. In the next subsection, we propose a method to estimate the localizations of the targets based on the measurements $\{\mathcal{D}_k\}_{k=1}^K$.

B. Stage II: Target Location Estimation

In Stage II, the CPU jointly estimates the locations of the targets by utilizing the bistatic range measurements $\{\mathcal{D}_k\}_{k=1}^K$ obtained in Stage I. As shown in Fig. 3, the coordinates of a target can only be determined when multiple bistatic ellipses intersect at one point. However, due to the measurement error of bistatic ranges as shown in (23), a common intersection of the ellipses is unlikely to exist. Therefore, an ML-based algorithm is proposed for target location in the following.

1) *Problem Formulation*: We firstly introduce a measurement error model as follows to approximate the intractable bistatic range (23):

$$\hat{d}_{k,j}^s = d_{k,j}^s + \varepsilon_{k,j}, \quad (26)$$

where $\varepsilon_{k,j} \sim \mathcal{CN}(0, \sigma_{k,j}^2)$ is the error for estimating $d_{k,j}^s$. Let $\mathcal{D}_k(t)$ denote the t -th largest element in set \mathcal{D}_k . In particular, we define $\mathcal{D}_k(0) = \emptyset$. Then, the matching between Target j and the range measurement $\mathcal{D}_k(f_{k,j})$ can be represented as a data association variable $f_{k,j} \in \{0, 1, \dots, |\mathcal{D}_k|\}$. Note that the correct matchings $\mathcal{F}^* = \{f_{k,j}^* \mid \forall k, j\}$ satisfying $\hat{d}_{k,j}^s = \mathcal{D}_k(f_{k,j}^*)$ is not known at the CPU. However, based on the measurement error model in (26), the probability distribution function of the event $\hat{d}_{k,j}^s = \mathcal{D}_k(f_{k,j})$, given \mathbf{q}_j and $f_{k,j}$, can be formulated as

$$p(\mathcal{D}_k(f_{k,j}) \mid \mathbf{q}_j, f_{k,j}) = \frac{1}{\sqrt{2\pi}\sigma_{k,j}} e^{-\frac{(\mathcal{D}_k(f_{k,j}) - \|\mathbf{q}_j\|_2 - \|\mathbf{q}_j - \mathbf{a}_k\|_2)^2}{2\sigma_{k,j}^2}}, \quad \forall k, j. \quad (27)$$

Define $\mathcal{Q} = \{\mathbf{q}_j \mid \forall j\}$, $\mathcal{F} = \{f_{k,j} \mid \forall k, j\}$ and $\mathcal{K}_j = \{k \mid f_{k,j} > 0\}$. Based on (27), the ML problem can be formulated as

$$\min_{\mathcal{Q}, \mathcal{F}} \sum_{j=1}^J \sum_{k \in \mathcal{K}_j} \frac{(\mathcal{D}_k(f_{k,j}) - \|\mathbf{q}_j\|_2 - \|\mathbf{q}_j - \mathbf{a}_k\|_2)^2}{2\sigma_{k,j}^2} \quad (28a)$$

$$\text{s.t. } \{0\} \cup \{f_{k,j} \mid \forall j\} = \{0, 1, 2, \dots, |\mathcal{D}_k|\}, \quad \forall k, \quad (28b)$$

$$f_{k,j} \neq f_{k,j'} \text{ if } f_{k,j} f_{k,j'} > 0, \quad \forall k, j \neq j'. \quad (28c)$$

The constraints (28b) and (28c) ensures that different bistatic ranges in \mathcal{D}_k are associated with different targets. Problem (28) is non-convex and difficult to solve. Nonetheless, given a feasible data association solution $\tilde{\mathcal{F}} = \{\tilde{f}_{k,j} \mid \forall k, j\}$ satisfying

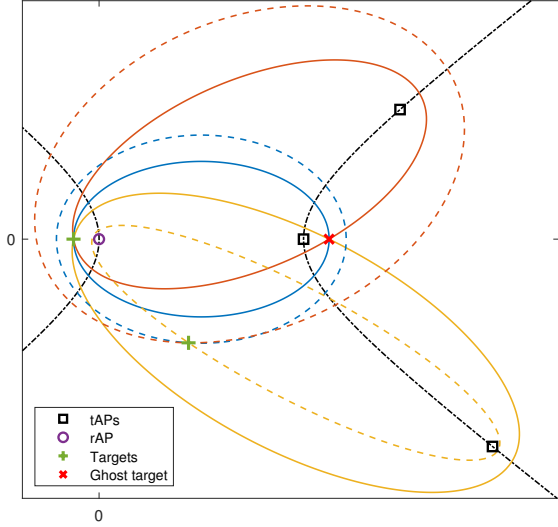


Fig. 4. An example with ghost target.

constraints (28b) and (28c), it can be transformed as

$$\min_{\mathbf{Q}} \sum_{j=1}^J \sum_{k \in \tilde{\mathcal{K}}_j} \frac{\left(\mathcal{D}_k(\tilde{f}_{k,j}) - \|\mathbf{q}_j\|_2 - \|\mathbf{q}_j - \mathbf{a}_k\|_2 \right)^2}{2\sigma_{k,j}^2}, \quad (29)$$

where $\tilde{\mathcal{K}}_j = \{k \mid \tilde{f}_{k,j} > 0\}$. Then, the optimal solution to Problem (29) can be obtained by separately solving J sub-problems, where the j -th subproblem is given by

$$\min_{\mathbf{q}_j} \sum_{k \in \tilde{\mathcal{K}}_j} \frac{\left(\mathcal{D}_k(\tilde{f}_{k,j}) - \|\mathbf{q}_j\|_2 - \|\mathbf{q}_j - \mathbf{a}_k\|_2 \right)^2}{2\sigma_{k,j}^2}. \quad (30)$$

Subproblem (30) is a non-linear least squared problem, which can be efficiently solved by Gauss-Newton algorithm [34]. Additionally, a closed-form solution for Problem (30) can be generated by spherical-intersection (SX) algorithm [35], providing a good initial value to ensure the convergence of Gauss-Newton algorithm. Nonetheless, the optimal data association solution \mathcal{F}^* cannot be found by the existing method except for exhaustive search, whose complexity is prohibitively high since there are $\prod_{k=2}^K \frac{J!}{(J-|\mathcal{D}_k|)!}$ feasible data association solutions, each of which corresponds to J subproblems as shown in (30). To address this issue, we propose a low-complexity algorithm for solving Problem (28) in the following.

2) *Rough Estimation*: In our considered device-free sensing scheme, all the target locations are estimated by using the bistatic ranges extracted from the reflected communication signals. In this case, the deployment locations of the APs may lead to estimation errors, even though the bistatic range measurements are precise. As illustrated in Fig 4, when the bistatic ellipses (marked with solid lines) have two common intersection points, a *ghost target* may be detected instead of the real one. In the following, we firstly introduce a lemma to show the sufficient conditions when there are no ghost targets in the bistatic location estimation:

Lemma 1: When there is no error in the measurement of bistatic ranges, a sufficient condition for ensuring a unique common intersection among multiple bistatic ellipses is that there does not exist a hyperbola where all tAPs lie on one branch while the rAP is located on the other.

Proof: We prove Lemma 1 by demonstrating its contrapositive, i.e., “When multiple bistatic ellipses have two or more common intersections, there must exist a hyperbola such that all tAPs lie on one branch and the rAP is located on the other.” Recall that the rAP is located at $(0, 0)$. Assuming that \mathbf{r}_1 and \mathbf{r}_2 are two of the common intersections, we have

$$\|\mathbf{r}_1 - \mathbf{a}_k\|_2 + \|\mathbf{r}_1\|_2 = \|\mathbf{r}_2 - \mathbf{a}_k\|_2 + \|\mathbf{r}_2\|_2, \quad \forall k. \quad (31)$$

Then, we have

$$\|\mathbf{r}_1 - \mathbf{a}_k\|_2 - \|\mathbf{r}_2 - \mathbf{a}_k\|_2 = -(\|\mathbf{r}_1\|_2 - \|\mathbf{r}_2\|_2), \quad \forall k. \quad (32)$$

The equations in (32) show that all tAPs are located on a branch of a hyperbola with \mathbf{r}_1 and \mathbf{r}_2 as foci, while the rAP is on the other branch. Hence, we arrive at the contrapositive of Lemma 1, and thus the proof is completed. ■

Lemma 1 provides engineering guidance for the deployment of APs in cooperative networks to avoid the appearance of ghost targets. In this work, we focus on the scenario that each target is within the ESA of at least three tAPs and the APs are appropriately deployed. In this case, the condition of the unique intersection given in Lemma 1 is assumed to be satisfied, which means only three bistatic range measurements are required for a rough location estimation. Therefore, we propose to firstly estimate the locations of \tilde{J} targets based on three measurement sets, denoted by \mathcal{D}_{c_1} , \mathcal{D}_{c_2} and \mathcal{D}_{c_3} , where c_1 , c_2 and c_3 are different elements in $\{1, 2, \dots, K\}$, \tilde{J} is the number of targets within the common ESA of the three tAPs. Let us define a combination $\mathcal{C} = \{c_1, c_2, c_3\}$. Note that the number \tilde{J} , which satisfies $0 \leq \tilde{J} \leq \min_{k \in \mathcal{C}} \{|\mathcal{D}_k|\}$, is not known a priori at the CPU. A method for determining it will be discussed in Remark 1.

Similar to Problem (29), given a feasible data association solution $\tilde{\mathcal{F}}_{\tilde{J}}^{(3)} = \{\tilde{f}_{k,j} \mid k \in \mathcal{C}, j \leq \tilde{J}\}$ that satisfies constraints (28b) and (28c), the rough estimation problem can be formulated as

$$\min_{\mathcal{Q}_{\tilde{J}}^{(3)}} \sum_{j=1}^{\tilde{J}} \sum_{k \in \mathcal{C}} \frac{\left(\mathcal{D}_k(\tilde{f}_{k,j}) - \|\mathbf{q}_j^{(3)}\|_2 - \|\mathbf{q}_j^{(3)} - \mathbf{a}_k\|_2 \right)^2}{2\sigma_{k,j}^2}, \quad (33)$$

where $\mathcal{Q}_{\tilde{J}}^{(3)} = \{\mathbf{q}_j^{(3)} \mid j \leq \tilde{J}\}$. Problem (33) can also be decoupled into \tilde{J} subproblems and solved by SX and Gauss-Newton algorithms. Define the objective function of Problem (33) as $G(\tilde{\mathcal{F}}_{\tilde{J}}^{(3)}, \mathcal{Q}_{\tilde{J}}^{(3)})$. After searching all the feasible $\tilde{\mathcal{F}}_{\tilde{J}}^{(3)}$'s, we select the solution that minimizes $G(\tilde{\mathcal{F}}_{\tilde{J}}^{(3)}, \mathcal{Q}_{\tilde{J}}^{(3)})$, denoted by $\{\tilde{\mathcal{F}}_{\tilde{J}}^{(3)*}, \mathcal{Q}_{\tilde{J}}^{(3)*}\}$, as the rough estimation of the \tilde{J} targets.

Remark 1: Let us define the estimated bistatic range corresponding to tAP k and its location estimation \mathbf{q}_j as follows

$$\bar{d}_k^s(\mathbf{q}_j) = \|\mathbf{q}_j\|_2 + \|\mathbf{q}_j - \mathbf{a}_k\|_2. \quad (34)$$

To determine the true value of \tilde{J} , we propose to initialize it

as $\min_{k \in \mathcal{C}} \{|\mathcal{D}_k|\}$. After $\{\tilde{\mathcal{F}}_j^{(3)*}, \mathcal{Q}^{(3)*}\}$ is obtained, we can calculate the following indicator

$$\zeta \left(\tilde{\mathcal{F}}_j^{(3)*}, \mathcal{Q}^{(3)*} \right) = \max_{\tilde{f}_{k,j}^* \in \tilde{\mathcal{F}}_j^{(3)*}, \mathbf{q}_j^{(3)*} \in \mathcal{Q}^{(3)*}} \left\{ \left| \mathcal{D}_k \left(\tilde{f}_{k,j}^* \right) - \bar{d}_k^s \left(\mathbf{q}_j^{(3)*} \right) \right| \right\}. \quad (35)$$

Given a threshold ζ^{th} , the number of targets within the common ESA of the tAPs for $k \in \mathcal{C}$ is considered to be less than \tilde{J} if $\zeta \left(\tilde{\mathcal{F}}_j^{(3)*}, \mathcal{Q}^{(3)*} \right) > \zeta^{\text{th}}$. Then, we update the value of \tilde{J} as $\tilde{J} \leftarrow \tilde{J} - 1$ and repeat the above procedure until $\tilde{J} = 0$ or $\zeta \left(\tilde{\mathcal{F}}_j^{(3)*}, \mathcal{Q}^{(3)*} \right) \leq \zeta^{\text{th}}$.

3) *Accurate Estimation*: Based on the rough estimation $\mathcal{Q}^{(3)*}$, we can associate the \tilde{J} targets with the measured bistatic range $\hat{d}_{k,j}^s$'s corresponding to other tAPs for accurate location estimation. Specifically, the data association solutions corresponding to $\{\mathcal{D}_k\}_{k \notin \mathcal{C}}$, denoted by $\tilde{\mathcal{F}}_j^{\text{rest}*} = \left\{ \tilde{f}_{k,j}^* \mid k \notin \mathcal{C}, j \leq \tilde{J} \right\}$, are set as follows

$$\tilde{f}_{k,j}^* = \begin{cases} 0, & \text{if } \min_{\hat{d}_{k,j}^s \in \mathcal{D}_k} \left\{ \left| \hat{d}_{k,j}^s - \bar{d}_k^s \left(\mathbf{q}_j^{(3)*} \right) \right| \right\} > \zeta^{\text{th}} \\ \arg \min_x \left\{ \left| \mathcal{D}_k(x) - \bar{d}_k^s \left(\mathbf{q}_j^{(3)*} \right) \right| \right\}, & \text{otherwise,} \end{cases} \quad k \notin \mathcal{C}, j \leq \tilde{J}. \quad (36)$$

Then, the full data association for the \tilde{J} targets is given by

$$\tilde{\mathcal{F}}_j^* = \tilde{\mathcal{F}}_j^{(3)*} \cup \tilde{\mathcal{F}}_j^{\text{rest}*}. \quad (37)$$

By substituting $\tilde{\mathcal{F}}_j^*$ into Problem (29), we can obtain an accurate location estimation for the \tilde{J} targets, denoted by $\mathcal{Q}_j^* = \left\{ \mathbf{q}_j^* \mid j \leq \tilde{J} \right\}$.

Last, the associated bistatic ranges, $\left\{ \mathcal{D}_k \left(\tilde{f}_{k,j}^* \right) \right\}_{\tilde{f}_{k,j}^* \in \tilde{\mathcal{F}}_j^*}$, are eliminated from the measurement set \mathcal{D}_k 's. Then, we can change the combination \mathcal{C} and repeat the above steps until all targets are localized.

4) *Algorithm Development*: Based on the above discussion, the ML-based algorithm is proposed for target localization by solving Problem (28), the details of which are summarized in Algorithm 1. Note that with a larger number of range measurements in $\{\mathcal{D}_k\}_{k \in \mathcal{C}(t)}$, more targets are expected to be localized at the t -th iteration of Algorithm 1. Therefore, to reduce the total iterations required for estimating all target localizations, in Step 1, the tAPs and \mathcal{D}_k 's are re-indexed such that $|\mathcal{D}_1| \geq |\mathcal{D}_2| \geq \dots \geq |\mathcal{D}_K|$, and the combination \mathcal{C} 's are numbered such that $\sum_{k \in \mathcal{C}(t)} k \leq \sum_{k \in \mathcal{C}(t+1)} k$.

The complexity of Algorithm 1 is significantly reduced as compared with the exhaustive search method. On the one hand, the search overhead of Algorithm 1 is lower. Recall that the total number of feasible data association solution $\tilde{\mathcal{F}}$'s over which the exhaustive search method searches is $\prod_{k=2}^K \frac{J!}{(J-|\mathcal{D}_k|)!}$. By contrast, Algorithm 1 searches over $\frac{\prod_{k \in \mathcal{C}} |\mathcal{D}_k|!}{\tilde{J}! \prod_{k \in \mathcal{C}} (|\mathcal{D}_k| - \tilde{J})!}$ data association solution $\tilde{\mathcal{F}}_j^{(3)*}$'s to estimate the locations of \tilde{J} targets each time. Although the value of \tilde{J} may be determined in an iterative manner, the total number of searches is effectively reduced in most cases. On the other

Algorithm 1 Target Location Estimation Algorithm

Input: $\{\mathcal{D}_k\}_{k=1}^K$, $\{\mathbf{a}\}_{k=1}^K$, J and the threshold ζ^{th} .

Output: The estimation of the targets' location \mathcal{Q}^* .

- 1: **Initialization:** Re-index the tAPs and \mathcal{D}_k 's; Obtain all the possible combination \mathcal{C} 's of c_1 , c_2 and c_3 ; Define $\mathcal{C}(t)$ as the t -th combination; Set $\mathcal{Q}^* = \emptyset$ and $t = 1$.
 - 2: **for all t do**
 - 3: $\tilde{J} \leftarrow \min \{ \min_{k \in \mathcal{C}(t)} \{ |\mathcal{D}_k| \}, J - |\mathcal{Q}^*| \}$;
 - 4: **while** $\tilde{J} \geq 1$ **do** \triangleright Rough Estimation
 - 5: Solve Problem (33) over all feasible $\tilde{\mathcal{F}}_j^{(3)*}$ to obtain $\tilde{\mathcal{F}}_j^{(3)*}$ and $\mathcal{Q}^{(3)*}$;
 - 6: Calculate $\zeta \left(\tilde{\mathcal{F}}_j^{(3)*}, \mathcal{Q}^{(3)*} \right)$ via (35);
 - 7: **if** $\zeta \left(\tilde{\mathcal{F}}_j^{(3)*}, \mathcal{Q}^{(3)*} \right) > \zeta^{\text{th}}$ **then** $\tilde{J} \leftarrow \tilde{J} - 1$;
 - 8: **else Break;**
 - 9: **end if**
 - 10: **end while**
 - 11: **if** $\tilde{J} \geq 1$ **then** \triangleright Accurate Estimation
 - 12: Calculate $\tilde{\mathcal{F}}_j^*$ via (37);
 - 13: Solve subproblems in (30) given $\tilde{\mathcal{F}}_j^*$ to obtain \mathcal{Q}_j^* ;
 - 14: Eliminate $\left\{ \mathcal{D}_k \left(\tilde{f}_{k,j}^* \right) \right\}_{\tilde{f}_{k,j}^* \in \tilde{\mathcal{F}}_j^*}$ from \mathcal{D}_k 's;
 - 15: $\mathcal{Q}^* \leftarrow \mathcal{Q}^* \cup \mathcal{Q}_j^*$;
 - 16: **end if**
 - 17: **if** $|\mathcal{Q}^*| = J$ **then Break;**
 - 18: **end if**
 - 19: **end for**
-

hand, the complexity of solving Problem (33) is lower than that of solving J subproblems in (30) since $\tilde{J} \leq J$ and $3 \leq K$.

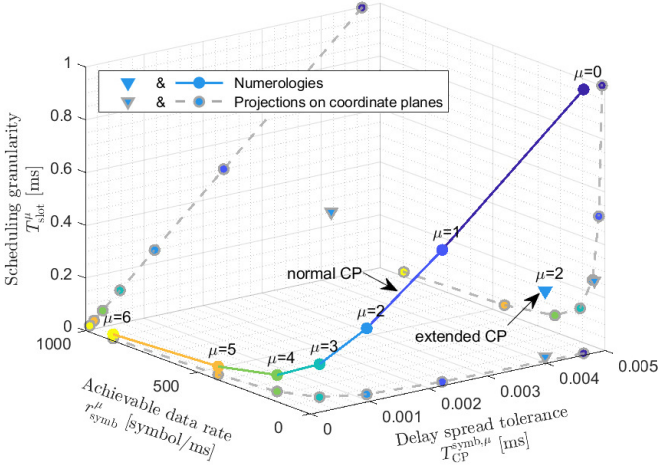
V. TRADE-OFF ANALYSIS AND SCENARIO EXTENSION

Based on the proposed sensing scheme for cell-free cooperative ISAC systems, this section analyzes the performance trade-offs achievable for both communication and sensing applications. Then, through certain modifications, the adaptability of the scheme to general scenarios is enhanced.

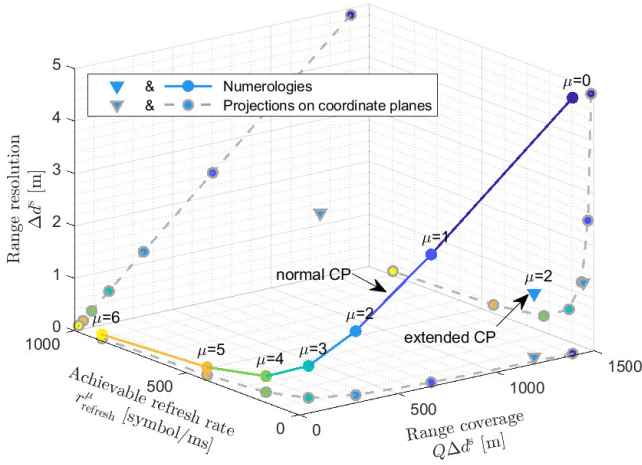
A. Performance Trade-offs

As mentioned in the system model, the proposed sensing scheme only utilizes the information-bearing signals received at the rAP, thus will not affect the communication performance. However, the flexible frame structure defined in the 5G standards introduced in Section II has paved the way for the trade-offs among a variety of KPIs for both applications. In the following, these trade-offs are discussed and compared for deeper insights into the cell-free cooperative ISAC systems. To facilitate the calculation of KPIs, we approximate the duration T_{CP}^{μ, l_s} and Q of the normal CP when $l_s \in \{0, 7\}$ to be equivalent to that when $l_s \notin \{0, 7\}$.

1) *Trade-offs in Communication*: A well-known trade-off in communication systems is the one between the throughput and the delay spread tolerance in transmission. On one hand, since the duration of an OFDM symbol is inversely proportional to the SCS Δf^μ , more symbols can be transmitted in a frame under the configurations with larger Δf^μ , leading to



(a) KPIs for communications versus the OFDM numerologies



(b) KPIs for sensing versus the OFDM numerologies

Fig. 5. Trade-off in communications and sensing.

a higher achievable data rate $r_{\text{syb}}^{\mu, \max}$ in terms of symbol/ms. On the other hand, the robustness of communication will significantly diminish when the maximum delay spread of the channel exceeds the duration of CP $T_{\text{CP}}^{\text{syb}, \mu}$. Thus, we can quantify the delay spread tolerance as $\Delta\tau^{\mu} = T_{\text{CP}}^{\text{syb}, \mu}$, which decreases as Δf^{μ} increases. In addition, scheduling granularity is a KPI for the resource allocation flexibility of cooperative transmission in the time domain. Note that the data transmission in each time slot can be scheduled independently based on the time slot formats [31]. Therefore, the scheduling granularity corresponding to SCS configuration μ can be quantified as the duration of each slot, denoted by T_{slot}^{μ} . In Fig. 5(a), the values of $\Delta\tau^{\mu}$, r_{syb}^{μ} and T_{slot}^{μ} are plotted for each OFDM numerology.

2) *Trade-offs in Sensing*: The main KPIs of sensing tasks affected by the OFDM numerologies are range coverage, achievable refresh rate and range resolution Δd^s . From (25), given a baseline range d_k^b , the range coverage of bistatic sensing corresponding to tAP k can be indicated by $Q\Delta d^s$. In this work, each set of bistatic range measurements \mathcal{D}_k is extracted

from a received OFDM symbol. Hence, the achievable refresh rate r_{refresh}^{μ} , i.e., the frequency at which the target location is estimated, is equal to the number of transmitted OFDM symbols per unit time. The values of the KPIs for sensing are shown in Fig. 5(b).

From Fig. 5, it can be summarized that there is a one-to-one correspondence between performance trade-offs in communication applications and sensing applications, both of which depend on the OFDM numerology. Specifically, an increase in μ leads to improvements in throughput, resource allocation flexibility, refresh rate, and range resolution, but it has performance loss in delay spread tolerance and coverage capability. Moreover, the extended CP introduces additional DoF for optimizing the aforementioned trade-offs. From Table II, when considering the SCS configuration with $\mu = 2$, it can be observed that the extended CP scheme exhibits an approximately fourfold increase in CP duration compared to the normal CP scheme. This elongation also leads to a reduction in the number of symbols in each time slot from 14 to 12. In other words, the selection of the CP mode facilitates a trade-off in ISAC systems, whereby a sacrifice of 1/7 in throughput and refresh rate enables an enhancement in the tolerance to delay spread and coverage capability. These trade-offs are achieved while preserving the resource allocation flexibility and range resolution.

Remark 2: In this subsection, we only focus on the performance trade-offs that can be achieved by using various OFDM numerologies. In practice, some KPIs can be enhanced by the cooperation among the APs. For example, as it will be shown in the simulation results, the range coverage of sensing can be significantly improved by increasing the number of APs in the system. In addition, the trade-off flexibility mentioned above may be constrained by various factors, such as the signal processing capabilities of UEs, because the number of signal samples requiring processing per unit time increases linearly with the SCS Δf^{μ} . Furthermore, new DoF for optimizing sensing KPIs can be introduced by minor updates in communication standards. For instance, from (2) and $\Delta d^s = c_0 T_s^{\mu}$, by increasing the FFT size N_f , the range resolution can be enhanced without affecting other communication or sensing KPIs.

B. Sensing Scheme for General Scenarios

In the previous derivations and discussions, we assume that all APs in the ISAC system apply the same configuration of SCS and CP. The communication requirements of UEs and the locations of the interested targets, however, can be time-space-varying. Therefore, cooperative ISAC systems can benefit from allowing each AP to switch between different OFDM numerologies independently. Furthermore, this improvement provides additional DoF for configuration of the system with multiple cooperative APs, achieving more flexible performance trade-offs in both communication and sensing applications. In this subsection, we extend our proposed scheme for target localization to a more general scenario with *hybrid numerology*, where the OFDM numerologies of the cooperative APs may be different.

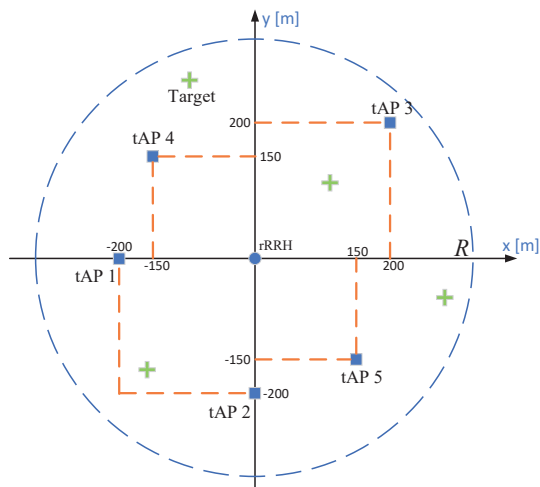


Fig. 6. Illustration of the APs' location in simulations.

Under the general scenarios, we denote the SCS configuration parameter of tRRH k and the corresponding bistatic range resolution as μ_k and Δd_k^s , respectively. It is worth noting that the framework introduced in Section IV remains applicable for target localization, even in cases where the range measurement $\{\mathcal{D}_k\}$'s exhibit diverse resolutions and range coverage. However, to ensure the optimal performance, we propose to modify certain steps in Algorithm 1:

1) *tAP and \mathcal{D}_k 's Re-indexing*: When the target locations are derived from measurements with higher resolutions, the estimation error is expected to reduce. Therefore, the set of the APs with small Δd_k^s 's should be prioritized to improve the sensing accuracy. Accordingly, at Step 1 of Algorithm 1, the tAPs and \mathcal{D}_k 's need to be re-indexed to satisfy the following inequalities for $\forall k \in \{1, 2, \dots, K-1\}$:

$$\Delta d_k^s \leq \Delta d_{k+1}^s, \quad (38)$$

$$|\mathcal{D}_k| \geq |\mathcal{D}_{k+1}|, \text{ if } \Delta d_k^s = \Delta d_{k+1}^s. \quad (39)$$

2) *Thresholds*: In Algorithm 1, a common threshold ζ^{th} is introduced to determine the values of \tilde{J} and $\tilde{f}_{k,j}^*$'s at steps 7 and 12, respectively. Due to variations in the resolutions of \mathcal{D}_k 's to be associated, different thresholds are required for rough estimation and accurate estimation in the scenarios with hybrid numerology. In this case, the threshold at Step 7 can be defined as a function $\zeta_{\text{Rou}}^{\text{th}}$ w.r.t. the set $\{\Delta d_k^s | k \in \mathcal{C}(t)\}$. Similarly, when calculating each $\tilde{f}_{k,j}^*$ in (36) at Step 12, the threshold ζ^{th} can be replaced by a function $\zeta_{\text{Acc}}^{\text{th}}$ w.r.t. Δd_k^s .

VI. SIMULATION RESULTS

In this section, numerical examples are presented to investigate the performance of the proposed cell-free cooperative ISAC scheme.

A. Simulation Setup

Fig. 6 illustrates the simulated cooperative ISAC scenario, where five predetermined locations of tAPs are plotted. The coordinates of the tAPs are set to that of tAP 1- K in Fig. 6 when simulating a scenario with K tAPs. Furthermore, the

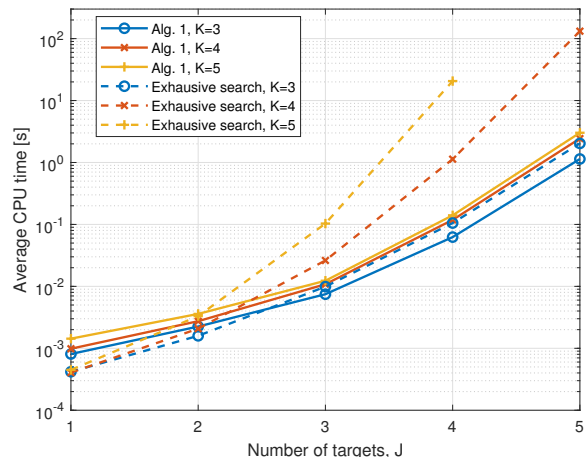


Fig. 7. CPU time of Algorithm 1 and exhaustive search method versus the number of targets J .

targets are randomly and uniformly generated within a circular area with a radius of R m, while the rAP is placed at the centre of the circle. Unless stated otherwise, the value of R is set to 400.

In the simulation, the bistatic range measurements $\{\mathcal{D}_k\}_{k=1}^K$ are firstly obtained based on (23), and the localization of the targets are estimated by solving Problem (28). We set the threshold $\zeta^{\text{th}} = 2\Delta d^s$ for Algorithm 1. The localization accuracy is defined as the ratio of the number of successful localizations to the number of all generated targets, where a localization is considered to be successful if the estimated location of the target is within a range of Δd^s from the true location. The simulation results are obtained by averaging over at least 10^5 independent target generations. As shown in Table II, when normal CP is applied, the CP duration Q of the most symbols is 288. Therefore, we only consider these symbols for simplicity.

B. Efficiency of Proposed Algorithm

As discussed in Section IV-B4, the complexity of the proposed Algorithm 1 for solving Problem (28) is lower than that of the exhaustive search method. In Fig. 7, we compare the average CPU time of the two algorithms in estimating the target locations under the setup of $K = 3, 4$, and 5 tAPs. Note that the y-axis is plotted on a logarithmic scale. It can be observed that when the number of targets J is less than 2, the CPU time of the exhaustive search method is slightly shorter. However, when J is relatively large, Algorithm 1 is more efficient. Furthermore, the gap in efficiency between the two algorithms increases significantly as K and J increase. When $K = 5$ and $J = 5$, more than 99% computational overhead can be saved by Algorithm 1. This indicates the superiority of the proposed Algorithm 1 in multi-target localization tasks within collaborative networks.

C. Coverage Capability

Based on 10^8 independent target realizations, Fig. 8 shows the coverage capability of the considered cooperative ISAC

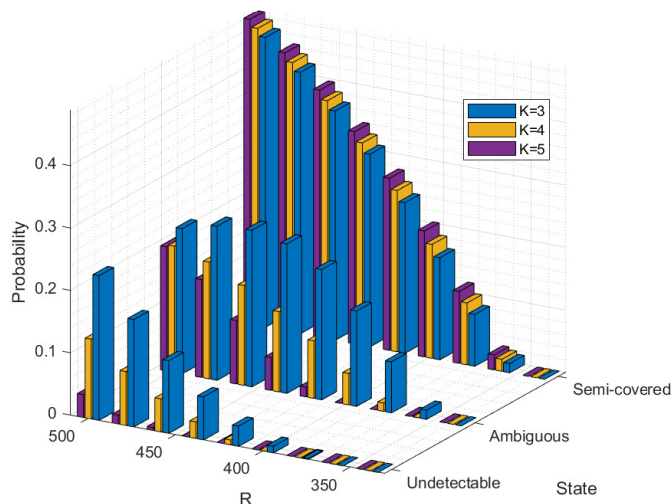


Fig. 8. Coverage capability of the considered schemes.

system versus the number of the tAPs K and the radius R . Specifically, the probability of a target being in the following three states are plotted: 1) *Undetectable*: the target lies within the ESA of no more than one tAP; 2) *Ambiguous*: the target is within the ESAs of two tAP; 3) *Semi-covered*: the target is covered by the ESAs of fewer than K tAPs.

As expected, the probability of the targets being undetectable and ambiguous increases with the growth of R , since the randomly distributed targets are more likely to fall outside the ESA of the tAPs. However, it can be seen that this trend can be effectively mitigated by increasing the number of tAPs, which improves the sensing availability. This highlights the advantages of cooperative sensing networks based on multiple communication infrastructures. In addition, it can be observed that the targets are more likely to lie within only part of the ESAs as the number of tAPs K increases. Therefore, we do not assume in this work that each target is within the ESAs of all tAPs, thereby enabling the sensing range to expand with the increasing number of APs in the cooperative ISAC system.

D. Sensing Performance

In the following, we evaluate the sensing performance of the cooperative ISAC system under a typical case at sub-6G, where the SCS is $\Delta f^\mu = 30$ KHz and the corresponding bistatic range resolution is $\Delta d^s = 2.4414$ m. Note that Algorithm 1 is developed based on the approximation of bistatic range measurement in (26), in which the measurement error is modelled as a Gaussian random variable. To verify the effectiveness of this approximation, we set $\sigma_{k,j}^2 = \sigma^2$ for $\forall k, j$ and introduce two baseline schemes, where the bistatic range measurements $\{\mathcal{D}_k\}_{k=1}^K$ are generated following (26), rather than the true range model in (23). In addition, the exhaustive search is also introduced as an upper bound on the localization accuracy of the system, since the optimal data association solution \mathcal{F}^* for Problem (29) can be determined based on it.

Fig. 9 shows the localization accuracy achieved by Algorithm 1 and the baseline schemes with $\sigma^2 = 0.49$ and

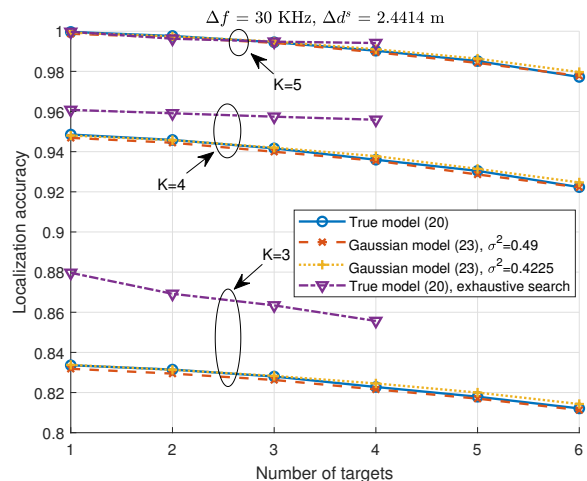


Fig. 9. Localization accuracy versus the number of targets J with SCS $\Delta f^\mu = 30$ KHz.

$\sigma^2 = 0.5625$. It is firstly noted that the accuracy achieved under the Gaussian-approximated models is almost the same as that under the true range model in all scenarios. Hence, the Gaussian model (26) is a good approximation for practical measurements. Secondly, it can be observed that Algorithm 1 achieves lower accuracy than the exhaustive search method when the number of tAPs K is small, due to a relatively high proportion of targets being in ambiguous state. Specifically, when a target is in ambiguous state, the exhaustive search method covers to one of the intersection points of the two bistatic ellipses, which may lead to a correct estimation. By contrast, Algorithm 1 is designed based on the assumption that each target is within the ESAs of at least three tAPs, and thus requires at least three bistatic ranges to generate a location estimation. However, when the network provides good coverage of the sensing service area ($K \geq 5$), the achieved accuracy of both algorithms is almost the same. Moreover, Fig. 9 shows that the localization accuracy is improved with the increase of K , which again verifies the performance gain of adding more tAPs. Finally, although the accuracy performance decreases as expected with an increasing number of targets J due to the increase in the probability of mismatching for bistatic range measurements, the decline is not significant as shown in Fig. 9. This validates the capability of the proposed cell-free cooperative ISAC system for multi-target localization.

In Fig. 10, we consider a configuration at FR2 with $\Delta f^\mu = 120$ KHz. Due to the lower range coverage of the system, the radius of the circular area is reduced to $R = 100$ m and the predetermined locations of tAPs (in m) are set as $(-50, 0)$, $(0, -50)$, $(50, 50)$, $(-35, 35)$ and $(35, -35)$. We can observe that the localization accuracy shown in Fig. 10 is similar to that in Fig. 9. Thanks to the improved bistatic range resolution, our proposed scheme exhibits an approximate accuracy of 98%, ensuring that the localization error in locating $J = 6$ targets does not exceed $\Delta d^s = 0.6104$ m under the scenario with $K = 5$ tAPs. It can be concluded that the proposed sensing scheme possesses good applicability across various transmission numerologies, and the range resolution is an ap-

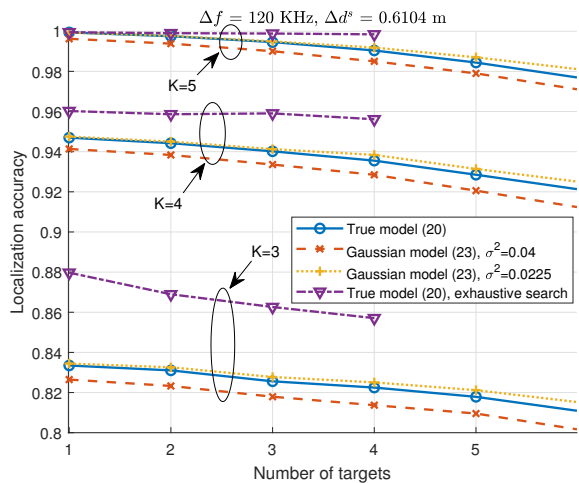


Fig. 10. Localization accuracy versus the number of targets J with SCS $\Delta f^\mu = 120$ KHz.

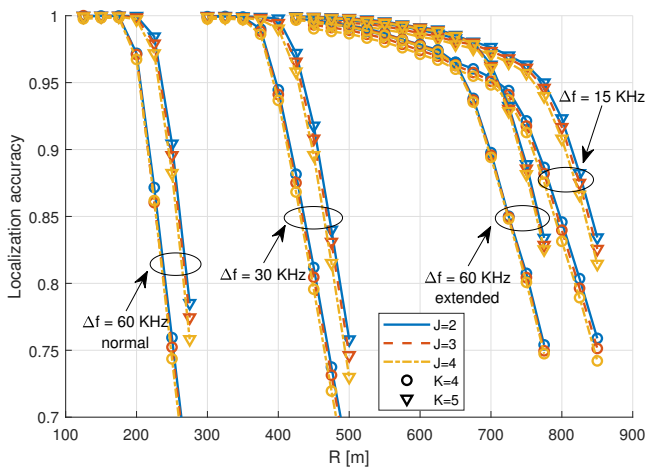


Fig. 11. Localization accuracy versus the radius R under different numerologies.

appropriate parameter to measure whether the location estimation is correct or not.

E. Coverage Capability versus OFDM numerologies

In order to analyze the coverage capability of the practical cooperative ISAC system under different OFDM numerologies, Fig. 11 depicts the variation of the achieved localization accuracy with the radius R of the target distribution area. Firstly, a “critical radius” can be seen for each numerology, whereby the accuracy experiences a drastic decrease when the radius R exceeds this value, indicating the maximum sensing range of the corresponding system. Secondly, it can be observed that as the SCS doubles, the maximum sensing range is approximately halved, which is consistent with the trade-off between range resolution and range coverage as shown in Fig. 5(b). Additionally, the configuration employing the extended CP represents a noteworthy case, exhibiting coverage capability close to that of the configuration with $\Delta f^\mu = 15$ KHz and normal CP.

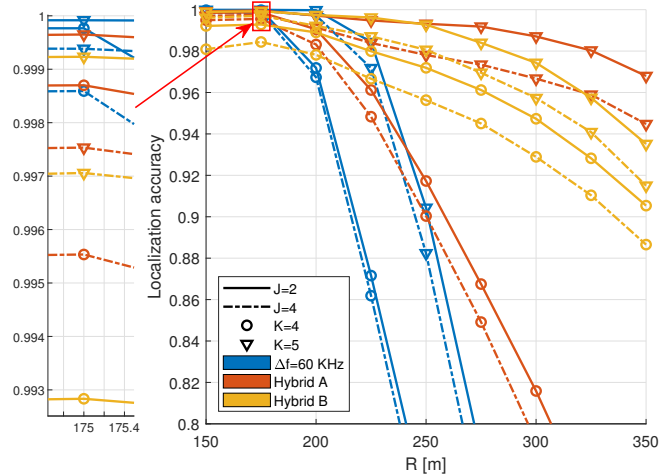


Fig. 12. Localization accuracy versus the radius R under hybrid numerologies.

F. Coverage Capability in General Scenarios

To verify the effectiveness of the modified Algorithm 1 designed in Section V-B, we consider two schemes with hybrid numerology, denoted by **Hybrid A** and **Hybrid B**, in the following. Specifically, the SCS configurations of the tAPs under **Hybrid A** and **Hybrid B** are set as $[\mu_1, \mu_2, \mu_3, \mu_4, \mu_5] = [2, 2, 1, 2, 1]$ and $[\mu_1, \mu_2, \mu_3, \mu_4, \mu_5] = [1, 2, 1, 2, 2]$, respectively. In addition, tAP 4 under both numerology schemes applies extended CP. Fig. 12 shows the localization accuracy achieved by the modified Algorithm 1, where the localization is considered to be successful when estimation error does not exceed 1.2207 m. A scenario is also evaluated as the performance baseline, where all tAPs are configured with $\Delta f = 60$ KHz and normal CP. In the simulation, the thresholds for the modified Algorithm 1 are set as $\zeta_{\text{Rou}}^{\text{th}} = 2 \cdot \max\{\Delta d_k^s | k \in \mathcal{C}(t)\}$ and $\zeta_{\text{Acc}}^{\text{th}} = 2\Delta d_k^s$. For the baseline scheme, this setup ensures that the performance of the modified Algorithm 1 is consistent with that of the original algorithm.

From Fig. 12, it can be overbed that when $R < 200$, the baseline scheme exhibits slightly higher localization accuracy than others. This is as expected due to the system’s robust coverage for targets and the fine resolution of range measurements. However, as R increases, the localization accuracy becomes constrained by the limited range coverage. In such cases, significant performance gain can be achieved by configuring the extended CP or a smaller SCS for a part of APs. Hence, ISAC systems supporting hybrid numerology offer potential for flexible performance trade-offs between localization accuracy and coverage capability, especially when the number of cooperative APs is large. Furthermore, we can see that when $K = 5$, **Hybrid A** and **Hybrid B** assign the same set of numerologies to different APs. The performance variance between them reflects the impact of numerology configuration strategy, which suggests a potential direction for future works.

VII. CONCLUSION

In this paper, we proposed a cooperative ISAC framework to integrate the sensing functionality into the cell-free MIMO networks, by leveraging the communication signal transmission of APs and information sharing at the CPU. We designed a two-stage scheme for the range measurement extraction and the target localization. In particular, an effective algorithm was proposed for joint range data association and location estimation of the targets. Based on the proposed sensing scheme and 5G NR frame structure, we also analyzed the performance trade-offs in practical cooperative ISAC systems. Considering the general scenarios with hybrid numerology, the sensing scheme was further modified to enable additional DoF for fine performance trade-offs. Simulation results demonstrated that the proposed sensing scheme achieves high localization accuracy and flexible performance trade-offs in the cooperative ISAC framework.

REFERENCES

- [1] Z. Wang, K. Han, J. Jiang, Z. Wei, G. Zhu, Z. Feng, J. Lu, and C. Meng, "Symbiotic sensing and communications towards 6G: Vision, applications, and technology trends," in *Proc. IEEE Veh. Technol. Conf.*, 2021, pp. 1–5.
- [2] F. Liu, C. Masouros, A. P. Petropulu, H. Griffiths, and L. Hanzo, "Joint radar and communication design: Applications, state-of-the-art, and the road ahead," *IEEE Trans. Commun.*, vol. 68, no. 6, pp. 3834–3862, Jun. 2020.
- [3] R. Di Taranto, S. Muppirisetty, R. Raulefs, D. Slock, T. Svensson, and H. Wymeersch, "Location-aware communications for 5G networks: How location information can improve scalability, latency, and robustness of 5G," *IEEE Signal Process. Mag.*, vol. 31, no. 6, pp. 102–112, Nov. 2014.
- [4] A. Hassani, M. G. Amin, E. Aboutanios, and B. Himed, "Dual-function radar communication systems: A solution to the spectrum congestion problem," *IEEE Signal Process. Mag.*, vol. 36, no. 5, pp. 115–126, Sep. 2019.
- [5] C. Sahin, J. Jakabosky, P. M. McCormick, J. G. Metcalf, and S. D. Blunt, "A novel approach for embedding communication symbols into physical radar waveforms," in *Proc. IEEE Radar Conf. (RadarConf)*, 2017, pp. 1498–1503.
- [6] D. K. Pin Tan, J. He, Y. Li, A. Bayesteh, Y. Chen, P. Zhu, and W. Tong, "Integrated sensing and communication in 6G: Motivations, use cases, requirements, challenges and future directions," in *Proc. IEEE Int. Online Symp. Joint Commun. Sens. (JC&S)*, 2021, pp. 1–6.
- [7] F. Liu, Y. Cui, C. Masouros, J. Xu, T. X. Han, Y. C. Eldar, and S. Buzzi, "Integrated sensing and communications: Toward dual-functional wireless networks for 6G and beyond," *IEEE J. Sel. Areas Commun.*, vol. 40, no. 6, pp. 1728–1767, Jun. 2022.
- [8] J. Yang, C.-K. Wen, S. Jin, and X. Li, "Enabling plug-and-play and crowdsourcing SLAM in wireless communication systems," *IEEE Trans. Wirel. Commun.*, vol. 21, no. 3, pp. 1453–1468, Mar. 2022.
- [9] X. Zhang, J. Wang, and Y. Qian, "Advances in cooperative wireless networking: Part I [guest editorial]," *IEEE Commun. Mag.*, vol. 49, no. 5, pp. 54–55, May 2011.
- [10] X. Tong, Z. Zhang, and Z. Yang, "Multi-view sensing for wireless communications: Architectures, designs, and opportunities," *IEEE Commun. Mag.*, vol. 61, no. 5, pp. 40–46, Dec. 2023.
- [11] H. Ren, N. Liu, C. Pan, and C. He, "Energy efficiency optimization for MIMO distributed antenna systems," *IEEE Trans. Veh. Technol.*, vol. 66, no. 3, pp. 2276–2288, 2017.
- [12] Y. Dai, W. Nam, T. Luo, and A. Kannan, "A cooperative device free wireless sensing design and analysis for target position estimation," in *Proc. IEEE Int. Conf. Commun. Workshops (ICC Workshops)*, 2022, pp. 830–835.
- [13] J. A. del Peral-Rosado, R. Raulefs, J. A. López-Salcedo, and G. Seco-Granados, "Survey of cellular mobile radio localization methods: From 1G to 5G," *IEEE Commun. Surv. Tutor.*, vol. 20, no. 2, pp. 1124–1148, Secondquarter 2018.
- [14] S. Aditya, O. Dizdar, B. Clerckx, and X. Li, "Sensing using coded communications signals," *IEEE open J. Commun. Soc.*, vol. 4, pp. 134–152, Dec. 2023.
- [15] H. Luo, Y. Wang, J. Zhao, H. Wu, S. Ma, and F. Gao, "Integrated Sensing and Communications in Clutter Environment," 2023. [Online]. Available: <https://arxiv.org/abs/2311.01674>
- [16] L. Liu and S. Zhang, "A two-stage radar sensing approach based on MIMO-OFDM technology," in *Proc. IEEE Globecom Workshops (GC Wkshps)*, Dec. 2020, pp. 1–6.
- [17] Z. Wei, Y. Wang, L. Ma, S. Yang, Z. Feng, C. Pan, Q. Zhang, Y. Wang, H. Wu, and P. Zhang, "5G PRS-based sensing: A sensing reference signal approach for joint sensing and communication system," *IEEE Trans. Veh. Technol.*, vol. 72, no. 3, pp. 3250–3263, Mar. 2023.
- [18] J. A. Zhang, X. Huang, Y. J. Guo, and M. L. Rahman, "Signal stripping based sensing parameter estimation in perceptive mobile networks," in *Proc. IEEE-APS Top. Conf. Antennas Propag. Wirel. Commun. (APWC)*, 2017, pp. 67–70.
- [19] Z. Wei, W. Jiang, Z. Feng, H. Wu, N. Zhang, K. Han, R. Xu, and P. Zhang, "Integrated sensing and communication enabled multiple base stations cooperative sensing towards 6G," *IEEE Netw.*, early access, Oct. 2023, doi:10.1109/MNET.2023.3321690.
- [20] S. Shi, Z. Cheng, L. Wu, Z. He, and B. Shankar, "Distributed 5G NR-based integrated sensing and communication systems: Frame structure and performance analysis," in *Proc. European Signal Process. Conf. (EUSIPCO)*, 2022, pp. 1062–1066.
- [21] H. Ren, N. Liu, C. Pan, M. ElKashlan, A. Nallanathan, X. You, and L. Hanzo, "Low-latency c-ran: An next-generation wireless approach," *IEEE Veh. Technol. Mag.*, vol. 13, no. 2, pp. 48–56, Apr. 2018.
- [22] M. L. Rahman, J. A. Zhang, X. Huang, Y. J. Guo, and R. W. Heath, "Framework for a perceptive mobile network using joint communication and radar sensing," *IEEE Trans. Aerosp. Electron. Syst.*, vol. 56, no. 3, pp. 1926–1941, Jun. 2020.
- [23] P. Gao, L. Lian, and J. Yu, "Cooperative ISAC with direct localization and rate-splitting multiple access communication: A pareto optimization framework," *IEEE J. Sel. Areas Commun.*, vol. 41, no. 5, pp. 1496–1515, May 2023.
- [24] M. Bashar, K. Cumanan, A. G. Burr, M. Debbah, and H. Q. Ngo, "On the uplink max-min SINR of cell-free massive MIMO systems," *IEEE Trans. Wireless Commun.*, vol. 18, no. 4, pp. 2021–2036, Apr. 2019.
- [25] Y. Cao and Q.-Y. Yu, "Joint resource allocation for user-centric cell-free integrated sensing and communication systems," *IEEE Commun. Lett.*, vol. 27, no. 9, pp. 2338–2342, Sep. 2023.
- [26] Q. Shi, L. Liu, S. Zhang, and S. Cui, "Device-free sensing in OFDM cellular network," *IEEE J. Sel. Areas Commun.*, vol. 40, no. 6, pp. 1838–1853, Jun. 2022.
- [27] Q. Wang, L. Liu, S. Zhang, and F. C. Lau, "Trilateration-based device-free sensing: Two base stations and one passive IRS are sufficient," in *Proc. IEEE Global Commun. Conf. (GLOBECOM)*, Dec. 2022, pp. 5613–5618.
- [28] Z. Wei, R. Xu, Z. Feng, H. Wu, N. Zhang, W. Jiang, and X. Yang, "Symbol-level integrated sensing and communication enabled multiple base stations cooperative sensing," *IEEE Trans. Veh. Technol.*, vol. 73, no. 1, pp. 724–738, Jan. 2024.
- [29] 3GPP, "5G; NR; physical channels and modulation," 3rd Generation Partnership Project (3GPP), Technical Specification (TS) 38.211, Jul. 2023, version 17.5.0. [Online]. Available: https://www.etsi.org/deliver/etsi_ts/138200_138299/138211/
- [30] —, "5G; NR; user equipment (UE) radio transmission and reception; part 1: Range 1 stand alone," 3rd Generation Partnership Project (3GPP), Technical Specification (TS) 38.101, Jul. 2023, version 17.10.0. [Online]. Available: https://www.etsi.org/deliver/etsi_ts/138100_138199/138101/
- [31] —, "5G; NR; physical layer procedures for control," 3rd Generation Partnership Project (3GPP), Technical Specification (TS) 38.213, Oct. 2023, version 17.7.0. [Online]. Available: https://www.etsi.org/deliver/etsi_ts/138200_138299/138213/
- [32] Y. Ming and L. Yi, "Model selection and estimation in regression with grouped variables," *J. Royal Statistical Society: Series B (Statistical Methodology)*, vol. 68, no. 1, pp. 49–67, Feb. 2006.
- [33] M. Grant and B. SP, "CVX: Matlab software for disciplined convex programming," <http://cvxr.com/cvx/>, Jan. 2020, version 2.2.
- [34] M. Gavish and A. Weiss, "Performance analysis of bearing-only target location algorithms," *IEEE Trans. Aerosp. Electron. Syst.*, vol. 28, no. 3, pp. 817–828, Jul. 1992.
- [35] M. Malanowski and K. Kulpa, "Two methods for target localization in multistatic passive radar," *IEEE Trans. Aerosp. Electron. Syst.*, vol. 48, no. 1, pp. 572–580, Jan. 2012.